electronics

MDPI

Article

Method for Classification and Optimization of Modes in Triple-Active-Bridge Converter Based on Waveform Structural Characteristics Analysis

Laiyong Zhang *, Chunming Tu, Fan Xiao, Bei Liu and Peiqiang Li

National Electric Power Conversion and Control Engineering Technology Research Center, Hunan University, Changsha 410082, China; chunming_tu@263.net (C.T.); woliaokk321@hnu.edu.cn (F.X.); beiliu@hnu.edu.cn (B.L.); lpqcs@hnu.edu.cn (P.L.)

* Correspondence: laiyong_zhang@hnu.edu.com

Abstract: The working mode classification of a triple-active-bridge converter (TAB) is the prerequisite and foundation of modulation optimization research based on time-domain analysis. Currently, systematic research on mode classification is lacking. Inadequate screening of mode types can lead to local optima, preventing the achievement of global optimal control. To address this issue, this paper proposes a mode classification method for the TAB converter based on waveform structural characteristics, enabling effective mode classification and specific mode screening. Firstly, time-domain modeling is carried out for the three square waves output from the three ports. Then, the entire waveform within one period is decomposed into various sub-mode combinations. Subsequently, by analyzing the permutation and combination rules of sub-modes corresponding to different waveforms, the construction method of the TAB working mode is derived, and then all working modes of TAB can be screened using an iterative optimization algorithm. Finally, on this basis, through the specific combination of sub-modes, not only the local optimal working mode with relatively low current stress or RMS value can be selected according to the waveform and energy transmission law, but also the working mode with port power decoupling function can be selected. This method has the advantages of clear classification, multidimensional characteristics and expansibility. It not only effectively classifies the modes of the TAB converter, but also selects the locally optimal working mode, particularly those with power decoupling modulation characteristics. Simulation and experimental results validate the correctness and effectiveness of the theoretical analysis.

Keywords: triple-active-bridge DC/DC converter; classification and optimization of modes; waveform structure characteristics; sub-mode; power decoupling modulation

check for updates

Academic Editor: Fabio Corti

Received: 11 November 2024
Revised: 24 December 2024
Accepted: 3 January 2025
Published: 5 January 2025

Citation: Zhang, L.; Tu, C.; Xiao, F.; Liu, B.; Li, P. Method for Classification and Optimization of Modes in Triple-Active-Bridge Converter Based on Waveform Structural Characteristics Analysis. *Electronics* **2025**, *14*, 187. https://doi.org/10.3390/electronics14010187

Copyright: © 2025 by the authors. Licensee MDPI, Basel, Switzerland. This article is an open access article distributed under the terms and conditions of the Creative Commons Attribution (CC BY) license (https://creativecommons.org/licenses/by/4.0/).

1. Introduction

The DC converter is a core device in DC power distribution networks, responsible for connecting grids of different voltage levels, controlling power flow, and regulating voltage. It plays a crucial role in ensuring the efficient and stable operation of the entire DC power distribution network [1,2]. Among the many topologies of DC converters, the triple active bridge converter has received significant attention and research owing to its numerous advantages, including multi-port capability, high power density, high conversion efficiency, flexible and controllable power direction, and electrical isolation [3,4]. The performance of the TAB converter directly influences the overall efficiency and stability of the connected system, thereby attracting considerable attention and in-depth research

from experts worldwide [5,6]. To enhance the efficiency, optimal control of TAB converter, particularly the optimal control of multiple phase shift modulation, has emerged as a focal research area in recent years [6,7].

Modeling of TAB multi-phase-shift modulation can be categorized into two approaches: frequency-domain analysis and time-domain analysis, each possessing unique characteristics. The frequency domain modeling of the TAB converter does not require mode classification, and the frequency domain function expressions of the unified optimization objectives and related parameters can be clearly established to facilitate direct optimization. However, in practical optimization, the frequency-domain functional expressions for relevant parameters such as voltage, current and power can only be composed of fundamental and limited harmonics, leading to inadequate parameter accuracy and impeding the formulation of the optimization program itself. Consequently, the accuracy of the optimization results is unsatisfactory [4,6,8]. Time-domain analysis can effectively address the issue of insufficient accuracy. It establishes accurate mathematical models and time domain function expressions for relevant parameters, facilitating the construction of optimization procedures and ensuring the precision of optimization results [9]. However, time-domain analysis requires classification of working modes and optimization of each mode, leading to substantial optimization efforts.

Mode classification is essential for modulation optimization research based on time-domain analysis. By optimizing all modes and thoroughly comparing the optimization results of each mode, the globally optimal control can be achieved. Incomplete mode classification can hinder a comprehensive comparison of optimization results, often leading to local optima and preventing the achievement of global optimal control. Therefore, accurately and comprehensively identifying all converter modes is a prerequisite and key to modulation optimization research based on time domain analysis.

Currently, there exists only a classification method for the working modes of the double active bridge (DAB), but this method is not extensible to TAB and other multi-port converters [9,10]. The classification of working modes in the triple-phase-shift modulation control of DAB, as discussed in [11–13], primarily depends on empirical or traversal methods. These methods can effectively address mode classification issues when dealing with fewer optimization variables and a limited number of working modes. The specific implementation involves separating the voltage square waves on both sides, fixing the square wave waveform on one side, and inserting the other square wave into the previous one in various combinations to identify 12 working modes through empirical or traversal methods. Nonetheless, this approach is only applicable to mode classification in extended phase-shift (EPS), dual phase-shift (DPS), and triple phase-shift (TPS) modulation of DAB, demonstrating limited generality [13–15].

A large number of different types of working modes are derived from mode classification methods. It will be a huge workload to optimize each mode one by one. Typically, all modes require targeted and efficient screening. In the research area of mode selection, [12,16] utilize graphical analysis to perform equivalent simplification of modes based on the waveform structural characteristics of DAB. This approach can equivalently simplify some modes into a locally optimal mode, thereby reducing the workload of optimization. The concept of the locally optimal mode encompasses two aspects:

(1) From the perspective of many different types of working modes, several exhibit lower current stress or RMS values compared to others within the power transmission range;

(2) From the perspective of the entire power transmission range, several working modes exhibit smaller current stress or RMS value than other working modes only in certain segments of the power transmission range, but not across the entire power range.

Based on the waveform structure and the real-time energy transmission relationship, [16,17] the mode in which both DAB square waveforms are simultaneously at high or low levels within a certain time period is selected as the local optimal mode. The selection mechanism and principles of these DAB local optimal modes are also applicable to the selection of local optimal modes for TAB and other multi-port converters. Nonetheless, this area remains unexplored in current research.

To address the limitations in existing research, this paper proposes a mode classification method for the TAB converter based on waveform structure feature analysis. Initially, this method models the three square waves of the TAB converter's ports in the time domain and then decomposes these waves into various sub-mode combinations in one period. Subsequently, by analyzing the arrangement and combination rules of sub-modes corresponding to different waveforms, we derive the construction method for the TAB working mode. Based on this construction method, different types of working modes are obtained by using repeated optimization algorithm. Finally, according to the laws of energy transmission and waveform structure, the locally optimal working modes of TAB are selected; on this basis, the decoupling modes are selected according to the decoupling waveform structure characteristics. The specific innovations are as follows:

(1) A method for classifying and selecting working modes based on the analysis of waveform structure features is proposed. By employing a repeated optimization algorithm to find all working mode types, the accurate classification of the working modes of TAB converter is realized. This method has the advantages of clear classification, multi-dimensional characteristics and scalability.

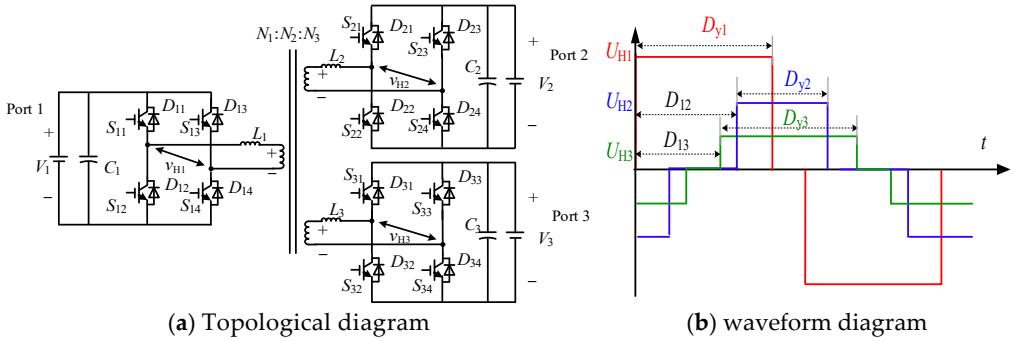
(2) Based on the intrinsic characteristics of sub-modes and their arrangement and combination rules, the locally optimal working modes of the TAB are first selected according to the laws of energy transmission and waveform structure. Subsequently, decoupled modes are screened out based on the waveform characteristics that meet the criteria for decoupled modulation.

2. Analysis of TAB Waveform Structure Characteristics

The TAB topology is shown in Figure 1a, which consists of three H-bridges, a three-winding high-frequency transformer and three auxiliary inductors containing the leakage inductance of the high-frequency transformer. As shown in the waveform diagram in Figure 1b, D_{y1}, D_{y2}, and D_{y3} denote the inner phase shift ratios, which represent the duty cycles of the high-level voltage in each H-bridge in half switching period. D_{12} and D_{13} represent the external phase shift ratios between two H-bridges, which correspond to the duty cycles of the phase shift angles between the rising edges of two square waves in half switching period. The magnitude and direction of power of the TAB are controlled by adjusting D_{y1}, D_{y2}, D_{y3}, D_{12} and D_{13}. Based on the TAB waveform structure, power transmission of TAB is achieved through the superposition of three square waves that share the same period, point symmetry, and different duty cycles.

As can be seen from Figure 2, the whole waveform of the TAB is composed of three square waves. In Figure 2, the sub-mode is defined as the operating mode in which the level of three square waves remains unchanged for a period of time in a cycle, and the operation mode in which the level of three square waves remain unchanged at single time point is defined as the point sub-mode. Due to central point symmetry, the sub-mode combinations in the first half of the cycle and the second half of the cycle are opposite to each other. The entire waveform in one cycle can be divided into a maximum of 12 sub-modes. In actual waveform, one period can also be decomposed into 10,8,6,4 or 2 sub-modes. It can be understood as the existence of several groups of adjacent identical sub-modes within the maximum number of sub-modes (12 sub-modes). When these adjacent sub-modes are

merged into one, it results in a reduction in the total number of sub-modes in one cycle. The working mode consisting of a maximum of 12 sub-modes is defined as the full working mode, while other working modes with fewer than 12 sub-modes are defined as non-full working modes. Since non-full working modes can be regarded as special cases of the full working mode, this paper concentrates on the full working mode as the research object.



(**a**) Topological diagram (**b**) waveform diagram

Figure 1. Topological and waveform diagram of TAB.

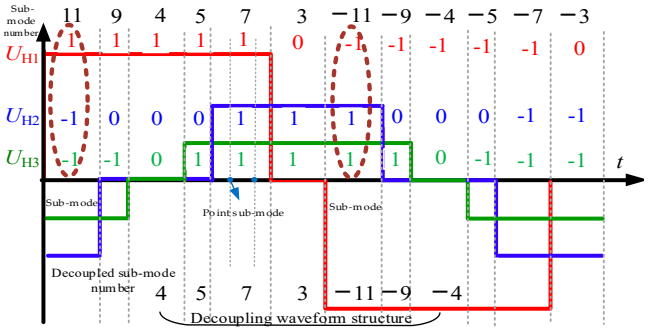


Figure 2. Waveform structure diagram of TAB working mode.

The type and number of sub-modes can be determined based on the level types of each square wave and the number of square waves. Since each square wave in the TAB has three level types (namely 0, −1, and +1) and there are three square waves, we obtain 3^3 (equivalently, 27) types of sub-modes, as shown in Table 1.

Table 1. Twenty-seven sub-modal types of TAB.

Sub-Mode Number	**0**	**1**	**2**	**3**	**4**	**5**	**6**	**7**	**8**	**9**	**10**	**11**	**12**	**13**
U_{H1}	0	0	0	0	1	1	1	1	0	1	1	1	−1	−1
U_{H2}	0	0	1	1	0	0	1	1	1	0	−1	−1	1	−1
U_{H3}	0	1	0	1	0	1	0	1	−1	−1	0	−1	−1	1
Sub-Mode Number		**−1**	**−2**	**−3**	**−4**	**−5**	**−6**	**−7**	**−8**	**−9**	**−10**	**−11**	**−12**	**−13**
U_{H1}		0	0	0	−1	−1	−1	−1	0	−1	−1	−1	1	1
U_{H2}		0	−1	−1	0	0	−1	−1	−1	0	1	1	−1	1
U_{H3}		−1	0	−1	0	−1	0	−1	1	1	0	1	1	−1

From the perspective of TAB's sub-modes, the working mode is composed of three square waves, U_{H1}, U_{H2}, and U_{H3}. Simultaneously, three ports generate three distinct levels. From the horizontal perspective (that is, from the time sequence), several sub-modes are selected from its 27 sub-mode types to arrange and combine regularly in a cycle, thus forming different types of working modes. The full working mode involves selecting

12 sub-modes from 27 sub-mode types for regular arrangement and combination. As illustrated in Figure 2, the three-dimensional working mode can be converted into a one-dimensional sub-mode number group by sub-mode numbering. This mode is represented by the sub-mode number group '11~9~4~5~3~−11~−9~−4~−5~−3', where the first half number and the second half number are opposite to each other.

According to the analysis of the waveform structure characteristics of the full working mode of TAB, the following rules are obtained:

(1) The high or low level (non-zero level) of a point-symmetric square wave can only appear once in one cycle. Similarly, the three levels corresponding to the three square waves in the TAB can only simultaneously be non-zero at most once in one cycle. Therefore, in the working mode, the sub-modes +/−7, +/−11, +/−12, and +/−13 can only appear at most once in one cycle, as indicated in the shaded part of Table 1.

(2) The three square waves share the same period and are point-symmetric. The sub-mode combination of the first half period and the sub-mode combination of the second half period are opposite to each other.

(3) In one cycle, only one of the three levels of the adjacent sub-modes changes, as shown in Figure 2.

(4) Multi-dimensional characteristics of sub-modes and their combinations: Both the sub-modes themselves and various combinations of sub-modes in the waveform structure have their own intrinsic meanings. For instance, Figure 2 shows a sub-mode combination labeled '4~5~7~3~−11~−9~−4' that represents a decoupling functional waveform characteristic.

3. Classification of TAB Working Modes

3.1. Time-Domain Modeling of Square Waves Based on Internal and External Phase Shift

The three square-wave time-domain modes of TAB are the prerequisite and basis for the study of its working mode classification. As shown in Figures 3 and 4, the whole waveform of TAB can be decomposed into three square waves.

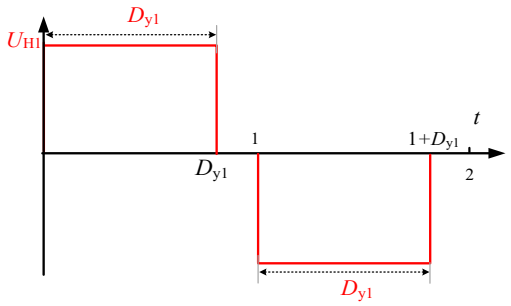


Figure 3. AC side square wave of port 1.

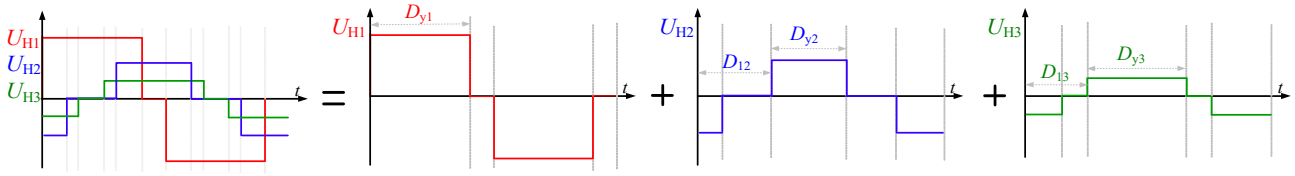


Figure 4. The waveform of TAB is decomposed into three square waves.

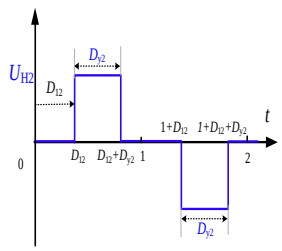
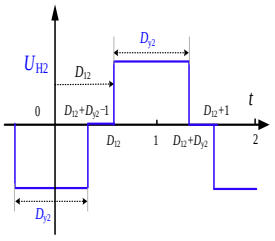
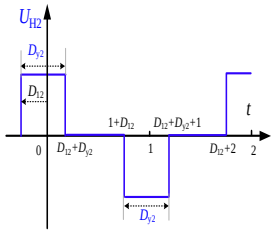
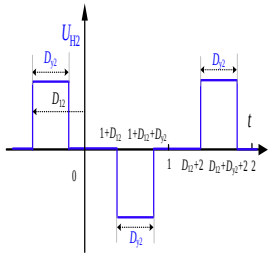
Figure 3 shows that U_{H1} of the TAB represents the square wave of port 1, which corresponds to the H-bridge AC side voltage. It comprises three different level types, namely 0, −1, and +1. The U_{H1} period T is defined as 2 and is centrosymmetric at point 1. Based

on the internal and external phase-shift angle duty cycles, the square wave time domain function expression is:

$$U_{H1} = \begin{cases} 1 & 0 \le t < D_{y1} \\ 0 & D_{y1} \le t < 1 \\ -1 & 1 \le t < D_{y1}+1 \\ 0 & D_{y1}+1 \le t < 2 \end{cases}$$

U_{H2} is the square wave of TAB port 2, which can be divided into four cases based on the value ranges of the internal and external phase-shift angle duty cycles, (D_{y2} and D_{12}). The types of U_{H2} square waves and their corresponding time-domain function expressions are presented in Table 2, where the period T of U_{H2} is defined as 2 and the U_{H2} square wave is centro-symmetric at point 1. The square wave U_{H3} of port 3 is similar to the square wave U_{H2} of port 2, with D_{13} and D_{y3} replacing D_{12} and D_{y2}, respectively. In practical applications, the type of square wave U_{H1} of port 1 in the TAB remains unchanged, while the types of square waves U_{H2} and U_{H3} of ports 2 and 3 are selected from the four types listed in Table 2 based on the set parameter ranges.

Table 2. Classification and time domain model of U_{H2}.

Type	1	2	3	4
range	$0 < D_{12} < 1, D_{12}+D_{y2} < 1$	$0 < D_{12} < 1, D_{12}+D_{y2} > 1$	$-1 < D_{12} < 0, D_{12}+D_{y2} > 0$	$-1 < D_{12} < 0, D_{12}+D_{y2} < 0$
graph				
function expressions	$U_{H2} = \begin{cases} 0 & 0 \le t < D_{12} \\ 1 & D_{12} \le t < D_{12}+D_{y2} \\ 0 & D_{12}+D_{y2} \le t < D_{12}+1 \\ -1 & D_{12}+1 \le t < D_{12}+D_{y2}+1 \\ 0 & D_{12}+D_{y2}+1 \le t < 2 \end{cases}$	$U_{H2} = \begin{cases} -1 & 0 \le t < D_{12}+D_{y2}-1 \\ 0 & D_{12}+D_{y2}-1 \le t < D_{12} \\ 1 & D_{12} \le t < D_{12}+D_{y2} \\ 0 & D_{12}+D_{y2} \le t < D_{12}+1 \\ -1 & D_{12}+1 \le t < 2 \end{cases}$	$U_{H2} = \begin{cases} 1 & 0 \le t < D_{12}+D_{y2} \\ 0 & D_{12}+D_{y2} \le t < D_{12}+1 \\ -1 & D_{12}+1 \le t < D_{12}+D_{y2}+1 \\ 0 & D_{12}+D_{y2}+1 \le t < D_{12}+2 \\ 1 & D_{12}+2 \le t < 2 \end{cases}$	$U_{H2} = \begin{cases} 0 & 0 \le t < D_{12}+1 \\ -1 & D_{12}+1 \le t < 1+D_{12}+D_{y2} \\ 0 & 1+D_{12}+D_{y2} \le t < D_{12}+2 \\ 1 & D_{12}+2 \le t < D_{12}+D_{y2}+2 \\ 0 & D_{12}+D_{y2}+2 \le t < 2 \end{cases}$

3.2. Classification Methods for Working Modes

In this paper, TAB is taken as the research object, and other multi-port DC converters can also be classified by similar methods. Firstly, the time-domain functions of the three square waves of the TAB are established. Then, by repeatedly changing the variable values (D_{y1}, D_{y2}, D_{y3}, D_{12}, and D_{13}) of the square wave functions, different types of three-square-wave combinations (that is, working modes) are generated in one cycle. From the perspective of sub-mode combinations: the essence of the three square waves of TAB is to select a number of sub-modes from the 27 sub-modal types in a cycle, and to arrange and combine them regularly to form a working mode. By constantly changing the value of the function variable, different types of working modes are obtained, and then all types of working modes can be obtained by repeated search and accumulation. A total of 480 types of the full working modes of TAB are identified by repeated optimization.

The flowchart of the repeated optimization method is shown in Figure 5. The main steps of its specific program implementation are as follows:

(1) Determination of point sub-mode type: The cycle is divided into 1000 time points. Based on a randomly generated set of three square waves (that is, the TAB variables D_{y1}, D_{y2}, D_{y3}, D_{12}, and D_{13} have fixed values), the three square wave level values at these 1000 time points are determined, that is, which of 0, −1 and +1 is determined. Further, the

sub-mode type (namely, point sub-mode type) that each time point belongs to is determined, as shown in Figure 6.

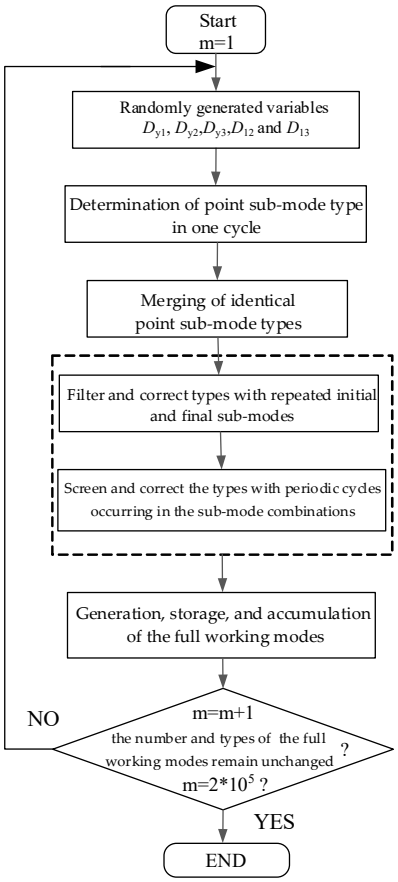


Figure 5. Flow chart of iterative optimization method for TAB working mode.

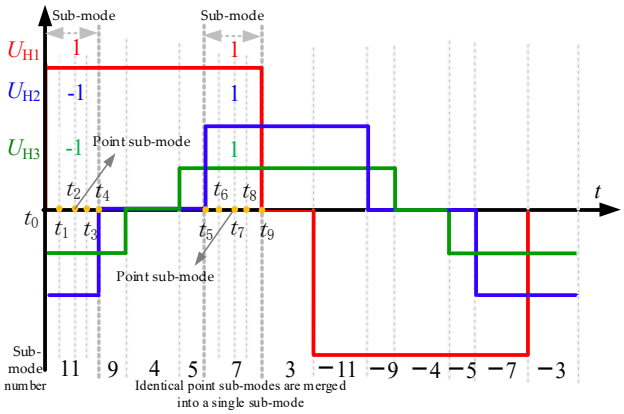


Figure 6. Point sub-mode and sub-mode in TAB.

(2) Merging identical point sub-mode types: When the sub-modal types of adjacent time points are the same, the adjacent time points are merged into a single time segment, resulting in different time segments with different sub-mode types, as shown in Figure 6. Thus, within one cycle, a set of three square waves can be represented by a regular arrangement and combination of a finite number of different types of sub-modes. This specific set of three square waves is a working mode. This mode can then be represented by a set of sub-mode numbers, as depicted in Figure 6.

(3) Filter and correct types with repeated initial and final sub-modes: Due to waveform periodicity, if the initial and final sub-mode types in a sub-mode combination are the same, delete the final sub-mode block to avoid repetition.

(4) Screen and rectify types with periodic cycles in the sub-mode combinations: When constructing working modes, to prevent periodic cycles within sub-modal combinations, based on the uniqueness of specific sub-modes from the three square waveform in the sub-modal combinations, sub-modes 7, 11–13, 8–10, 6, and 5 are sequentially set as the first sub-modes of the working mode. When the preferred sub-modal type 7 is unavailable, 11 is chosen as the new preferred sub-modal. When the sub-mode type 11 is unavailable, 12 is selected as the initial sub-mode, and this pattern of recursion continues.

(5) Generation, storage, and accumulation of the full working modes: By continuously changing the values of the TAB variables D_{y1}, D_{y2}, D_{y3}, D_{12}, and D_{13}, different types of three square waves are generated for the TAB, each corresponding to a unique sub-mode combination. Continuously search for the sub-mode combination with the maximum number of sub-modes in one cycle (namely, the full working mode), and continuously accumulate modes and eliminate duplicates to form a comprehensive set. This process continues until the number and types of elements in the comprehensive set remain unchanged and the iteration is updated 200,000 times. At this point, the comprehensive set represents the different types of the full working modes.

In this paper, we employed the repeated optimization method to identify 480 full working modes for the TAB. This approach can also be applied to determine the total number of full working modes for any multi-port DC-DC converter.

4. Principles and Methods for Optimizing Working Modes

In the face of the numerous working modes of the TAB converter, it would be a huge and tedious task to analyze and optimize each working mode one by one. To reduce the workload, this section introduces a criterion for judging the local optimal working mode, and then selects the working mode based on two different optimization principles, and validates the rationality of the optimization principle through the experimental program, and finally obtains the locally optimal working mode.

4.1. Evaluation Criteria for Local Optimal Working Modes

The primary criterion for comparing locally optimal modes with other modes is efficiency, a comprehensive metric defined as transmission power divided by the sum of transmission power and loss power. Its value largely hinges on the magnitude of loss power. The converter losses mainly include: (1) conduction losses, turn-on losses, and turn-off losses of the switching devices; (2) copper losses and iron losses in the high-frequency transformer and inductances [18,19]. These losses are closely related to the parameters such as the current RMS and current stress. The conduction losses of switching devices and copper losses in inductors and high-frequency transformers are positively correlated with the square of the current RMS. The turn-on and turn-off losses are positively correlated with current stress and switching frequency. Based on the above analysis, the evaluation criteria for the locally optimal working mode are current stress and current RMS.

4.2. Optimal Selection of Working Modes

By applying the mode classification method, numerous different types of working modes are obtained. Optimizing each mode one by one would entail a huge workload. Consequently, it is essential to effectively screen the modes based on the waveform characteristics of the TAB and specific requirements. This step significantly reduces the number of modes needing optimization, consequently decreasing the overall optimization burden.

①. Select the working modes containing sub -modes +/−7 preferentially.

The sub-mode +/−7 denotes the sub-mode where the voltage levels of the three terminals U_{H1}, U_{H2}, and U_{H3} are all +/−1. The working modes containing this sub-mode demonstrate unique performance attributes owing to their unique structure, as shown in Figure 7.

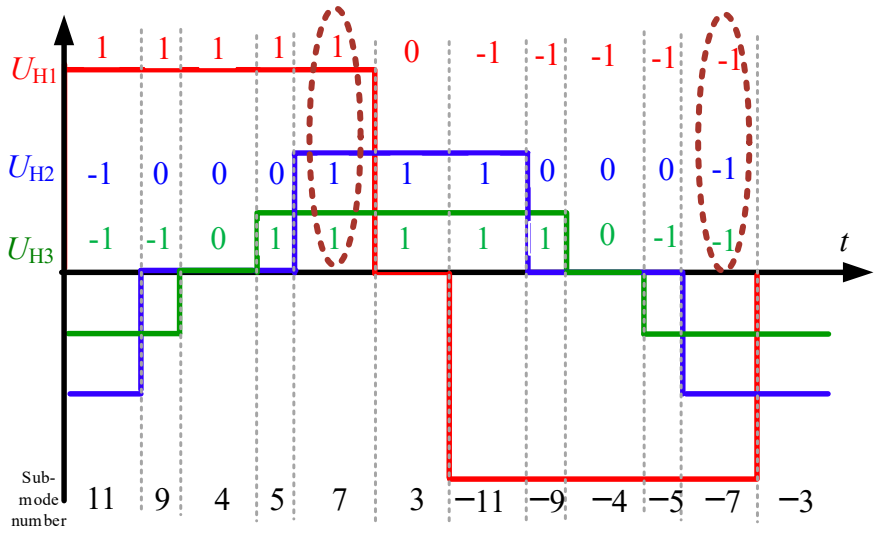


Figure 7. Triangular wave has high or low level at the same time.

Due to the similar topological structures of TAB and DAB, the mechanisms between their waveform structures and real-time energy transmission are identical. Based on the mechanism between DAB waveform structure and real-time energy transmission in [13,20], it can be obtained that in one switching cycle, when the voltage levels at both ends of the DAB are the same, that is, when they are both positive or negative levels simultaneously, the energy is directly transmitted from the input port to the output port, and will not stay and store in the converter; when the voltage levels at both ends are different, it means that energy cannot be directly transmitted at that moment and will be temporarily stored in the inductance of the converter. The stored energy is subsequently released from the inductance again and transmitted to the output port once the port voltage levels change. The period in which the energy temporarily stored in the inductor can significantly increase in the inductor current stress and RMS value, leading to higher losses. When a working mode contains sub-modes with voltage levels that are simultaneously positive or negative, its corresponding losses are relatively smaller compared to other working modes. Consequently, during the screening of working modes, preference is given to those exhibiting this characteristic [16]. Based on the above mechanism, as shown in Appendix A Table A2, the locally optimal modes 1.1, 1.2, 1.4, 2.1, 2.4, and 2.3 were selected from the 12 modes in DAB [16,20].

The mechanism and principles for optimizing working modes in DAB are also applicable to other multi-port DC converters, and thus can be applied to the optimization of TAB working modes as well. Figure 7 shows a working mode in TAB that contains the sub-mode +/−7. For the TAB converter, the local optimal working modes are preferentially selected as those where the voltage levels of the three terminals are simultaneously 1 or −1 (namely, containing the sub-mode +/−7). Consequently, this criterion results in the selection of 90 working modes out of the 480 available.

This section selects mode A-1.5/1.5/1.5 and mode B-1.1/1.5/1.2 that do not contain the sub-mode +/−7, mode 16-1.1/1.1/1.2 and mode 8-1.1/1.1/2.4 that contain the sub-mode +/−7, as shown in Appendix A Table A2. Using these four working modes as

examples, we validate the optimization principles through actual optimization results. In the TAB mode A-1.5/1.5/1.5, 'A' denotes the mode number, the first '1.5' represents the working mode of the equivalent DAB from port 1 to port 2, and similarly, the second and third '1.5's represent the working modes of the equivalent DABs from port 1 to port 3 and from port 2 to port 3, respectively. Firstly, experimental procedures are employed to optimize with the objectives of minimizing the current stress of the maximum power port (input port) and minimizing the sum of the squares of RMS values of the three ports, respectively. Then, the input port current stress and the sum of the squares of the RMS values of the three ports for these four working modes are compared under the same output powers P_2 and P_3, and with k_{12} and k_{13} set to 0.85 and 0.75, respectively.

In order to facilitate the analysis, the transmission power, current stress and the square sum of the RMS values of the three ports are normalized. The reference values for normalization are the reference power value $P_{\text{base}} = V_1^2/(4f_sL)$, the reference current value $I_{\text{base}} = V_1/(4f_s\,L)$, and the reference square sum of the RMS values $I^2_{\text{rms_base}} = (V_1/(4f_sL))^2$, where V_1 represents the voltage at input port 1, f_s denotes the switching frequency, and L is three times the inductance L_1 of the port. Unless otherwise stated, all figures and tables below refer to these three parameters in their normalized forms.

From Figure 8, it can be observed that under the optimization of the current stress of the maximum power port (input port), the stress and the RMS square sum of the three ports for modes 16 and 8, which contain the sub-mode $+/-7$, are both lower than those of the other two modes that do not contain the sub-mode $+/-7$ at the corresponding transmitted powers.

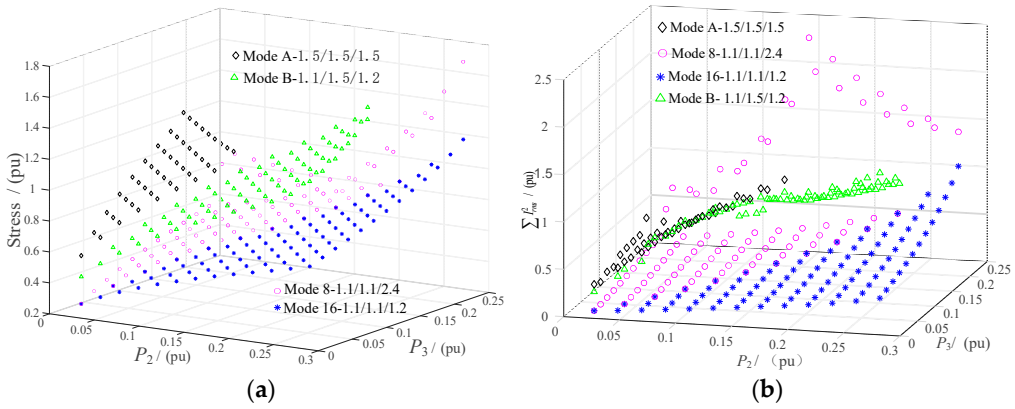


Figure 8. (**a**) Stress comparison at the maximum-power port in different modes under the optimization of the current stress of the maximum power port. (**b**) Comparison of the RMS square sum of the three ports in different modes under the optimization of the current stress of the maximum power port.

From Figure 9, which presents the optimization results for the sum of the squares of the RMS values at the three ports, it can be seen that the stress and the sum of the RMS square sum of the three ports for modes 16 and 8, which contain the sub-mode $+/-7$, are both lower than those of the modes that do not contain the sub-mode $+/-7$. From the above optimization results, it can be proved that the stress and the sum of the squares of RMS values of the working mode with sub-mode $+/-7$ in the same P_2 and P_3 and k_{12} and k_{13} is smaller than that of other working modes without sub-mode $+/-7$. This verifies the rationality of the proposed optimization mechanism and principles.

②. Select the working modes that meet the requirements of power decoupling modulation preferentially

By simplifying the TAB circuit structure and converting it to the primary side, its Y-type equivalent circuit can be obtained, as shown in Figure 10a. Further, through Y-Δ transformation, the Δ-type equivalent circuit shown in Figure 10b can be derived. At

this point, the TAB converter can be equivalent to three DAB converters, reducing the complexity of directly analyzing the TAB converter. Therefore, the optimization of the TAB converter can be equivalent to the optimization of three DAB converters.

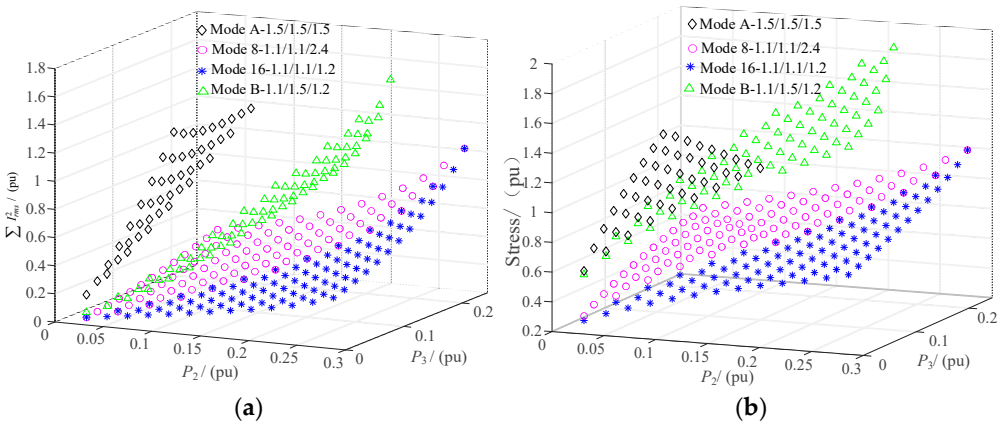


Figure 9. Flow chart of iterative optimization method for TAB working mode.

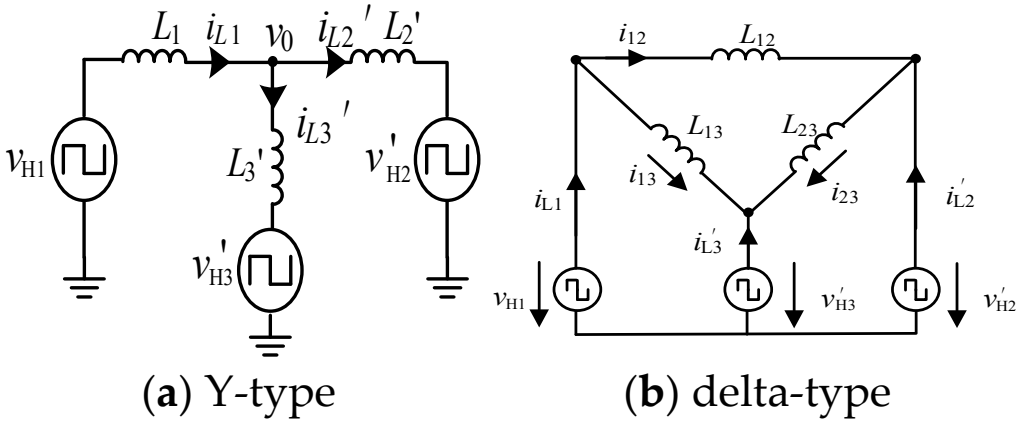


Figure 10. Y-type and delta-type equivalent circuit.

Figure 11 shows two operating conditions for the TAB: single-input dual-output and dual-input single-output. From Figure 11, it can be observed that there is power coupling between the dual output ports or the dual input ports. To reduce the coupling effect between its ports, this paper adopts a novel decoupling method called power decoupling modulation strategy. Distinct from other hardware and software decoupling, according to the rules of waveform structure, power decoupling of two input or output ports is achieved by modulation to make the center lines of the square waves of the two ports coincide (that is, to satisfy $D_{12} + 0.5D_{y2} = D_{13} + 0.5D_{y3}$), as shown in Figure 12. Compared with other decoupling methods, this method has the advantage of simple implementation.

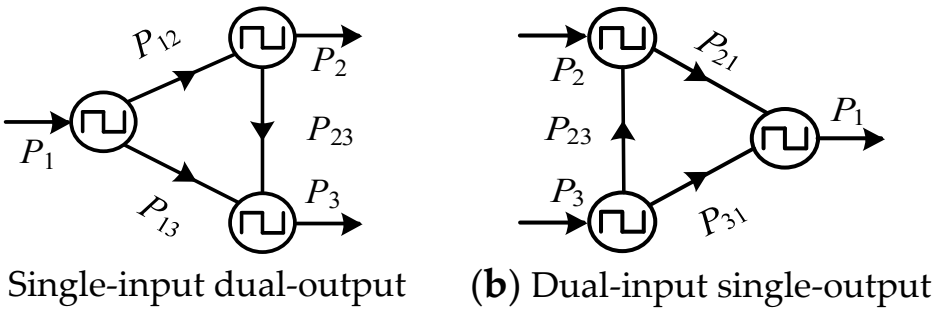


Figure 11. Single-input dual-output and dual-input single-output modes.

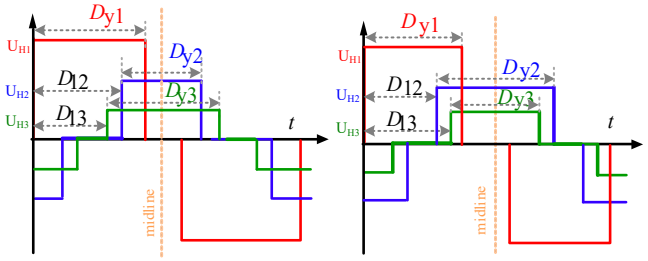


Figure 12. Voltage waveform under power decoupling phase shift control.

Power decoupling modulation mechanism: the two input or output ports of TAB can be considered equivalent to a DAB. Based on the mode classification and waveform characteristics of the DAB converter in Appendix A Table A2, the equivalent DAB in TAB is actually a special mode combination type in DAB converter working mode 2.4 or 1.2, as shown in Figure 13. Figure 13a presents a special modal combination in DAB mode 2.4 characterized by zero power transmission; Figure 13b shows a special modal combination in DAB mode 1.2, also featuring zero power transmission. In this state, during half of the cycle, the midlines of the two square waves align, with the current is symmetrically centered around the intersection of the midline and the horizontal axis. As illustrated in Figure 13, due to the symmetry of the current within the voltage square wave, the forward power and the reverse power are equal in magnitude but opposite in direction over one control cycle, resulting in a total sum of zero. Similarly, it can be deduced that the transmission power between two input or output ports of TAB under power decoupling modulation is 0, as shown in Figure 14. From the perspective of transmitted power, the TAB converter under decoupling modulation can be simplified and represented equivalently as two DABs. Optimized control of these two DABs is equivalent to optimizing the TAB, simplifying mode analysis and reducing optimization control difficulty. To meet the requirements of TAB power decoupling modulation, the combination of several sub-modes in the waveform structure must satisfy the equation $D_{12} + 0.5D_{y2} = D_{13} + 0.5D_{y3}$. This selection criterion enables the identification of 30 working modes with power decoupling modulation characteristics from the 90 selected modes, as presented in Table 3 and Appendix A Table A3.

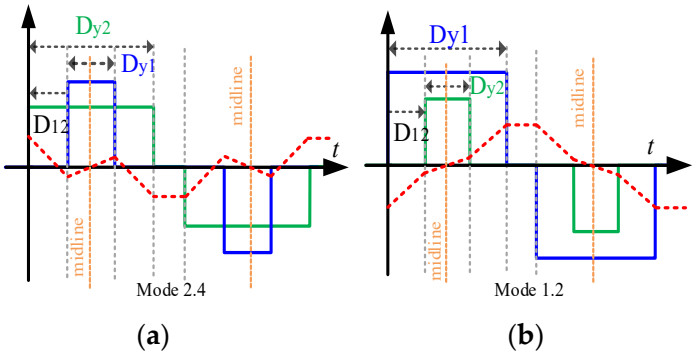


Figure 13. Waveforms under special mode combinations of DAB (**a**) mode 2.4 and (**b**) mode 1.2.

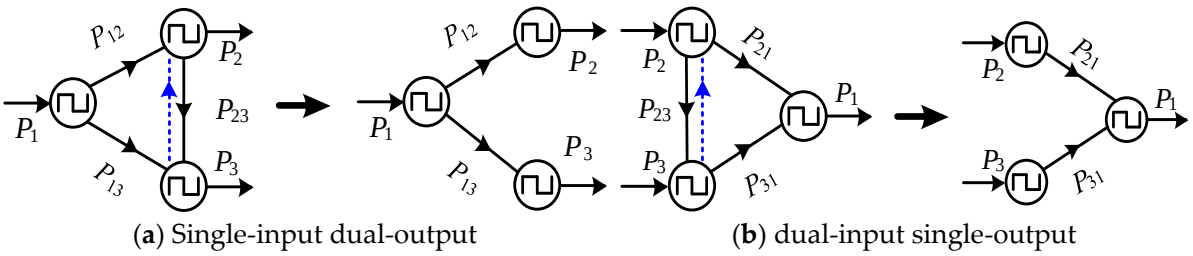
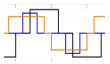
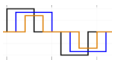
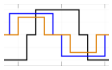
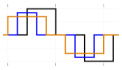
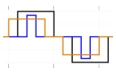
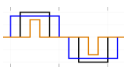
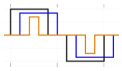
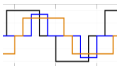
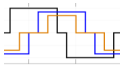


Figure 14. TAB power decoupling is equivalent to 2 DABs.

Table 3. DAB equivalence and waveform diagram of TAB working mode (1).

Mode Number	1→2 Equivalent DAB Mode	1→3 Equivalent DAB Mode	2→3 Equivalent DAB Mode	Waveform Port 1: Black/High Port 2: Blue/Mid Port 3: Yellow/Low	Mode Number	1→2 Equivalent DAB Mode	1→3 Equivalent DAB Mode	2→3 Equivalent DAB Mode	Waveform Port 1 : Black/High Port 2: Blue/Mid Port 3: Yellow/Low
1	2.1	2.3	2.4		16	1.1	1.1	1.2	
2	2.3	2.3	1.2		17	2.1	2.1	2.4	
3	1.2	2.1	2.4		18	2.4	1.2	1.2	
4	2.1	2.1	1.2		19	1.1	1.2	1.2	
5	1.1	1.4	2.4		20	1.4	1.4	1.2	
.	….	….	…	……	….	……	……	….	……

5. Experimental Verification and Analysis

To verify the effectiveness and feasibility of the proposed TAB mode optimization principles, this paper conducts validation through an experimental platform. The relevant main experimental parameters are shown in Table 4.

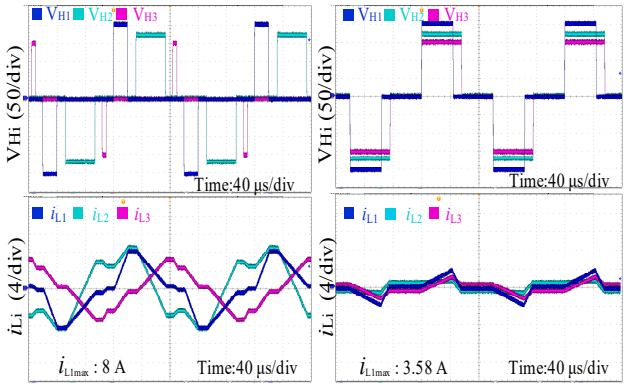
Table 4. Experiment parameters of TAB converter.

Parameter	Value
Voltage of port 1	200 V
Voltage of port 2	100–200 V
Voltage of port 3	40–200 V
Switching Frequency	5000 Hz
Transformer Turns Ratio	1:1:1
Additional Inductance of port 1, 2, 3	0.333 mH
Switching devices/MOSFET	MSC015SMA070B
Controller	TMS320F28335

5.1. Comparison of Working Modes With and Without Sub-Modes +/−7 Under Two Optimization Objectives

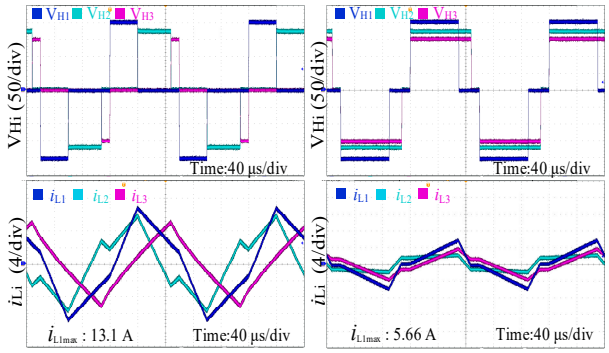
In this section, we compare the current stress of the maximum power port and the sum of the squares of the RMS values of the three ports under certain power conditions. This comparison is conducted for working modes both with and without sub-modes +/− 7, using the current stress of the input port and the sum of the squares of the RMS values of the three ports as the optimization objectives, respectively.

(1) As shown in Figures 15 and 16 and Table 5, under the stress of maximum power port (input port) optimization at different transmission powers, the current stresses and the sum of the squares of the RMS values of working modes 16 and 8, which include the sub-modes +/−7, are both lower than those of Mode A, which does not include the sub-modes +/−7. As shown in Figures 17 and 18 and Table 6, the current stress and the sum of the squares of the RMS values of working mode 16, which includes sub-mode +/−7, are lower than those of mode B, which does not include sub-mode +/−7, at different transmission powers. From the above, it can be concluded that working modes with the sub-modes +/−7 exhibit characteristics of lower stress and sum of the squares of the RMS values compared to other modes during the stress of input port optimization.



(**a**) Mode A-1.5/1.5/1.5 (**b**) Mode 16-1.1/1.1/2.4

Figure 15. Comparison of two modes under stress of input port optimization, when P_2 = 0.0425, P_3 = 0.0375.

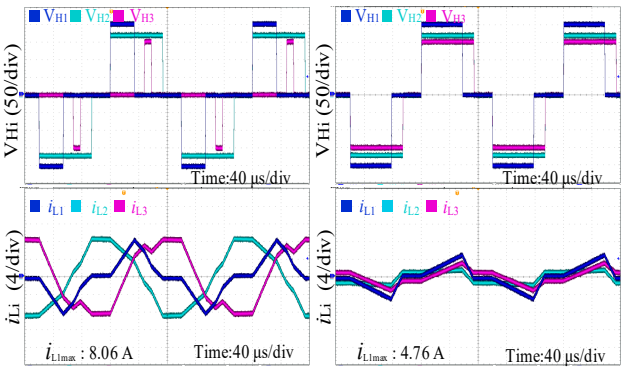


(**a**) Mode A -1.5/1.5/1.5 (**b**) Mode 8 -1.1/1.1/1.2

Figure 16. Comparison of two modes under stress of input port optimization, when P_2 = 0.10625, P_3 = 0.09375.

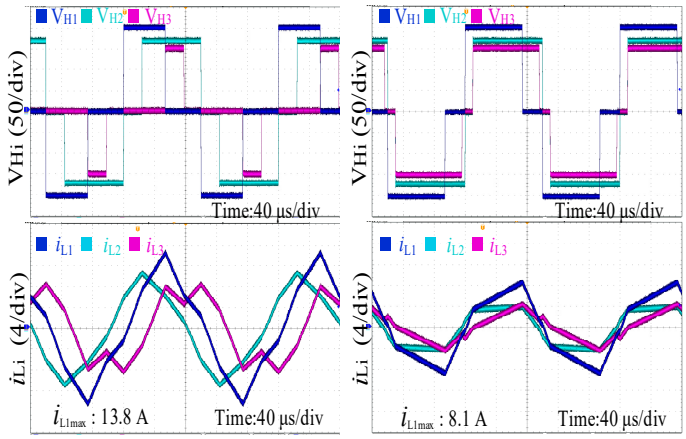
Table 5. Comparison of stress and RMS of different modes under stress of input port optimization.

P_2/P_3 (pu)	Mode A	Mode 16	Mode 8
	$I_{stress}/\sqrt{\sum I_{rms}^2}$ (A)		
0.0425/0.0375	8/7	3.58/2.1	
0.10625/0.09375	13.1/9.34		5.66/3.96



(**a**) Mode B-1.1/1.5/1.2 (**b**) Mode 16-1.1/1.1/2.4

Figure 17. Comparison of two modes under stress of input port optimization, when P_2 = 0.085, P_3 = 0.05625.



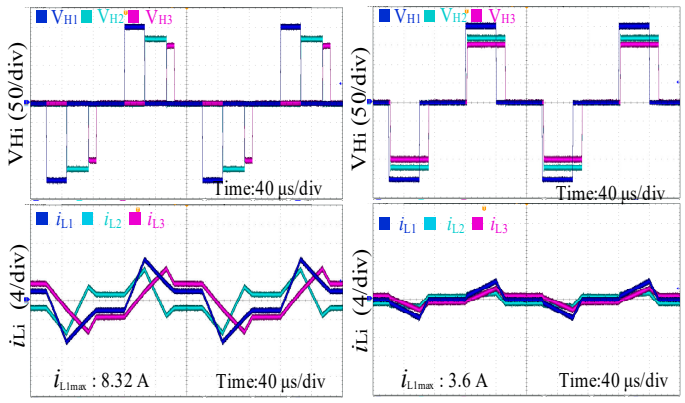
(**a**) Mode B-1.1/1.5/1.2 (**b**) Mode 16-1.1/1.1/2.4

Figure 18. Comparison of two modes under stress of input port optimization, when P_2 = 0.255, P_3 = 0.1125.

Table 6. Comparison of stress and RMS of different modes under stress of input port optimization.

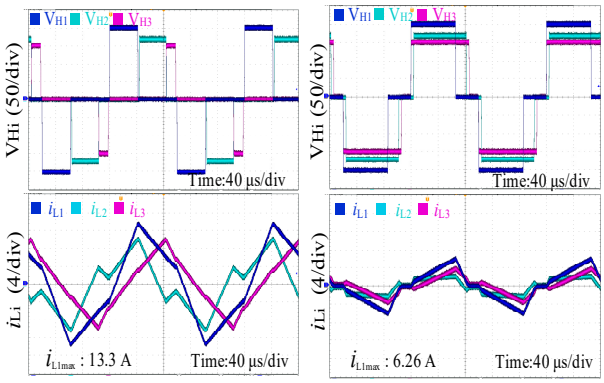
P_2/P_3 (pu)	Mode B	Mode 16
	$I_{stress}/\sqrt{\sum I_{rms}^2}$ (A)	
0.085/0.05625	8.06/9.14	4.76/3.14
0.255/0.1125	13.86/11.02	8.1/6.56

(2) As shown in Figures 19 and 20 and Table 7, under the optimization of minimizing the sum of the squares of the RMS values at different transmission powers, the current stresses and sum of the squares of the RMS values of working modes 16 and 8, which include the sub-modes +/−7, are both lower than those of Mode A, which does not include the sub-modes +/−7. As shown in Figures 21 and 22 and Table 8, the current stress and the sum of the squares of the RMS values of the working mode containing sub-mode +/−7 are lower than those of mode B, which does not contain sub-mode +/−7, at different transmission powers. From the above, it can be concluded that working modes with the sub-modes +/−7 exhibit characteristics of lower stress and the sum of the squares of the RMS values during the optimization of minimizing the sum of the squares of the RMS values.



(**a**) Mode A-1.5 + 1.5 + 1.5 (**b**) Mode 16-1.1 + 1.1 + 2.4

Figure 19. Comparison of the two models under the optimization of the square sum of RMS, when P_2 = 0.0425, P_3 = 0.0375.

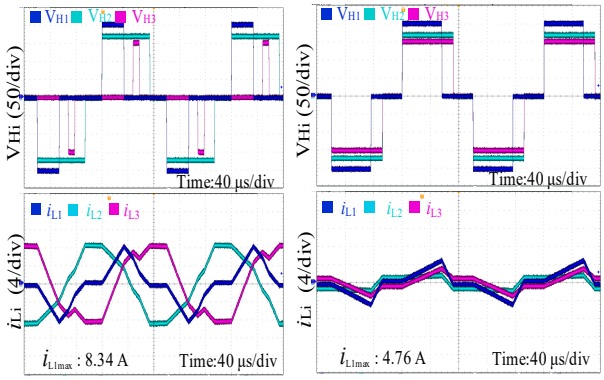


(**a**) Mode A-1.5/1.5/1.5 (**b**)Mode 8- 1.1/1.1/1.2

Figure 20. Comparison of the two models under the optimization of the square sum of RMS, when P_2 = 0.10625, P_3 = 0.09375.

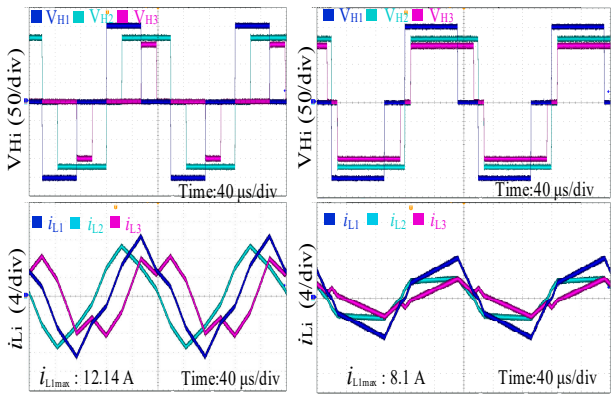
Table 7. Comparison of stress and RMS of different modes under the optimization of the square sum of RMS.

P_2/P_3 (pu)	Mode A	Mode 16	Mode 8
		$I_{stress}/\sqrt{\sum I_{rms}^2}$ (A)	
0.0425/0.0375	8.32/6.38	3.6/2.1	
0.10625/0.09375	13.32/11.38		6.26/3.9



(**a**) Mode B- 1.1/1.5/1.2 (**b**) Mode 16- 1.1/1.1/2.4

Figure 21. Comparison of the two models under the optimization of the square sum of RMS, when P_2 = 0.0825, P_3 = 0.05675.



(**a**) Mode B-1.1/1.5/1.2 (**b**) Mode 16-1.1/1.1/2.4

Figure 22. Comparison of the two models under the optimization of the square sum of RMS, when P_2 = 0.225, P_3 = 0.1125.

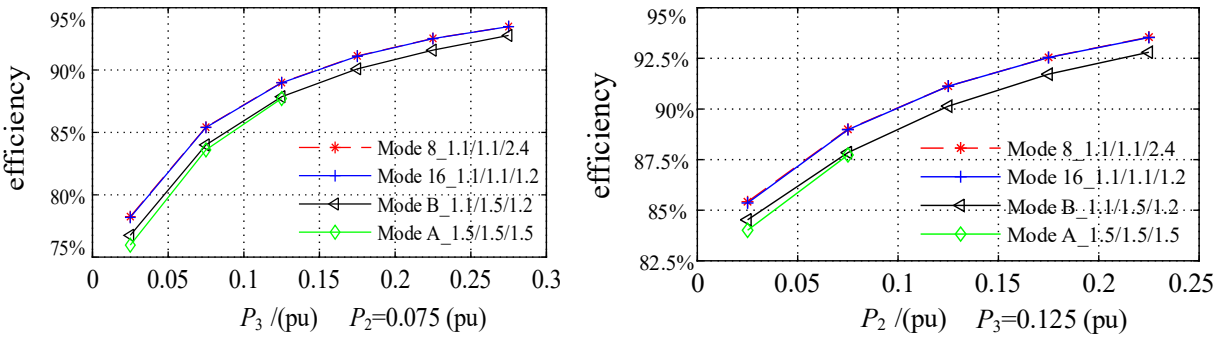
Table 8. Comparison of stress and RMS of different modes under the optimization of the square sum of RMS.

P_2/P_3 (pu)	Mode B	Mode 16
	$I_{stress}/\sqrt{\sum I_{rms}^2}$ (A)	
0.085/0.05625	8.34/8.98	4.76/3.14
0.255/0.1125	12.14/11.78	8.1/6.56

In summary, the stress and the sum of the squares of the RMS values of the working modes with sub-modes +/−7 under the two optimizations are lower than those of the working modes without sub-modes +/−7, which is consistent with the optimization principle in Section 4 of the paper.

5.2. Efficiency Comparison of Different Modes Under Two Optimization Methods

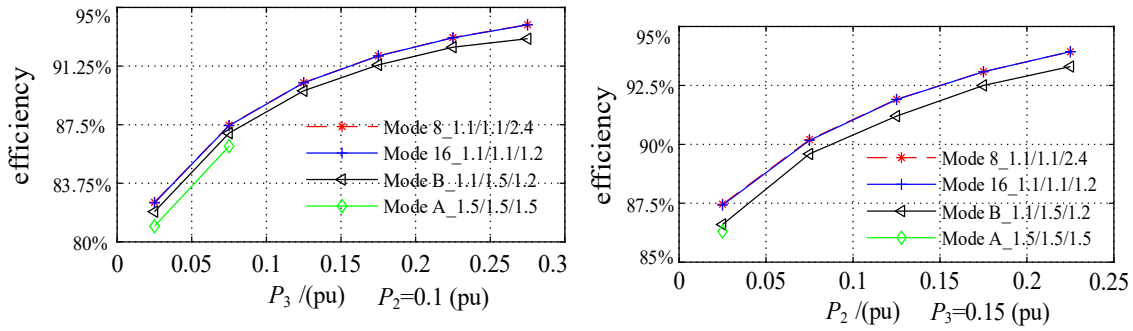
The efficiencies of various modes are compared under two conditions: the current stress of maximum power port optimization and three-port RMS square sum optimization, using an experimental platform. With transformation ratios k_{12} and k_{13} set at 0.85 and 0.75, respectively, we compared the efficiency of each mode at various power points under the same output power of different modes. To obtain the efficiencies at corresponding power points, we fixed the transmission power of one port and continuously varied the other. In the maximum power port optimization scenario, P_2 of port 2 was fixed at 0.075 (pu), while P_3 of port 3 varied continuously. The efficiencies at different power points in various modes were compared, as shown in Figure 23a. Likewise, with the P_3 of port 3 fixed at 0.125 (pu) and the P_2 of port 2 changes continuously, the efficiencies at different power points for different modes are compared, as illustrated in Figure 23b.



(**a**) P_2 = 0.075 and P_3 varies (**b**) P_3 = 0.125 and P_2 varies

Figure 23. Efficiency comparison of different modes at various power points under maximum power port current stress optimization.

Similarly, under the three-port RMS square sum optimization, the P_2 of port 2 is fixed at 0.1 (pu), and the power P_3 of port 3 changes continuously. The efficiencies of different power points in different modes are compared, as shown in Figure 24a. The P_3 of port 3 is fixed at 0.15 (pu), and the P_2 of port 2 changes continuously. The efficiencies of different power points in different modes are compared, as shown in Figure 24b. From Figures 1 and 2, it can be seen that the efficiencies of modes 8 and 16 with sub-mode +/−7 are higher than that of modes A and B without sub-mode +/−7 at different power points under the two optimization methods. This indicates that modes with sub-mode +/−7 have an advantage over those that do not, aligning with the theoretical analysis presented in Section 4. Therefore, during mode selection, preference is given to modes with sub-mode +/−7.



(**a**) P_2 = 0.1 and P_3 varies (**b**) P_3 = 0.15 and P_2 varies

Figure 24. Efficiency comparison of different modes at various power points under the optimization of the RMS sum of squares of the three ports.

6. Conclusions

This paper analyzes the waveform structure characteristics of TAB, summarizes its inherent laws and mode formation mechanisms, and subsequently proposes a method for mode classification and optimization. According to the inherent laws and mechanisms, the working modes based on the time domain are classified, and 480 full working modes are obtained by repeated search optimization. Based on the inherent rules of the TAB waveform structure and energy transmission, 90 locally optimal modes with lower stress or the sum of the squares of the RMS values are selected. According to the specific requirements of decoupling modulation, 30 decoupling modes are further screened out. Through theoretical research and experimental verification, we conclude that the following:

(1) Based on the characteristics of the waveform structure, the repetitive search optimization method can effectively identify all working modes of the TAB and is applicable to other multi-port DC converters.

(2) Based on the inherent rules of waveform structure and energy transmission, the mode optimization principles can effectively screen out the locally optimal modes of TAB. Additionally, by considering decoupling requirements, the decoupling modes can be selected, which significantly reduces the number of optimization modes and the optimization workload.

Author Contributions: Writing—original draft, L.Z.; Writing—review & editing, C.T., F.X., B.L. and P.L. All authors have read and agreed to the published version of the manuscript.

Funding: This research was funded by National Natural Science Foundation of China, grant number 52130704.

Data Availability Statement: The original contributions presented in this study are included in the article. Further inquiries can be directed to the corresponding author.

Conflicts of Interest: The authors declare no conflict of interest.

Appendix A

Table A1. Various working modes of DAB converter [16].

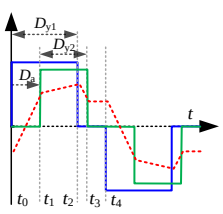
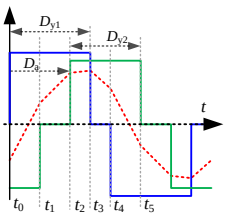
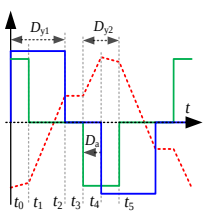
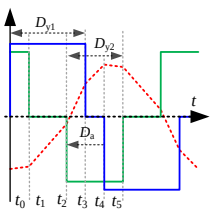
	Mode 1.1	Mode 1.4	Mode 2.1	Mode 2.3
Waveform				

Table A1. *Cont.*

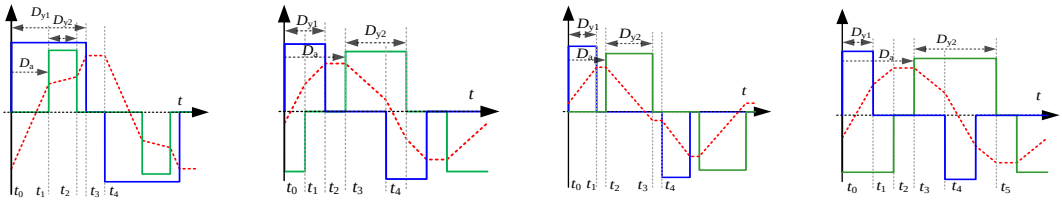
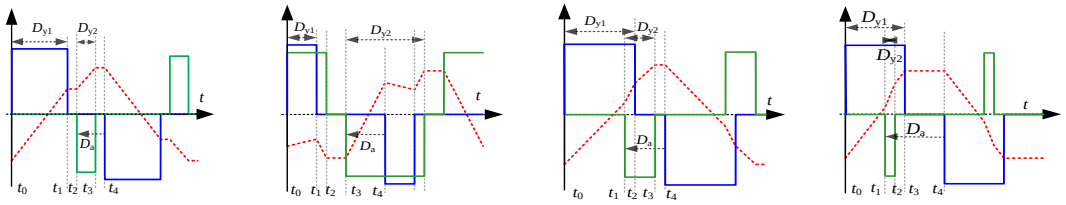
$D_a \geq 0$	Mode 1.2	Mode 1.3	Mode 1.5	Mode 1.6
Wave-form				
$D_a < 0$	Mode 2.2	Mode 2.4	Mode 2.5	Mode 2.6
Wave-form				

Table A2. Various working modes of single-input dual-output forward transmission from high voltage to medium and low voltage.

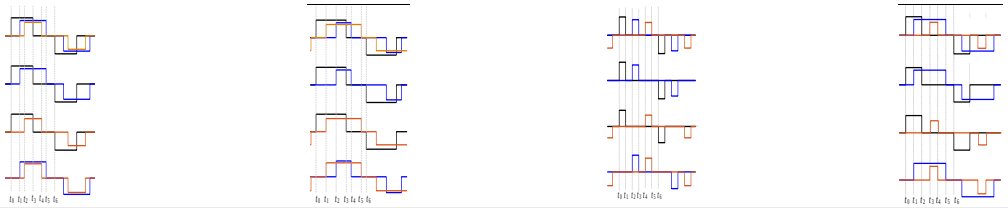
ForwardTransmission	Mode 16-1.1/1.1/1.2	Mode 8-1.1/1.1/2.4	Mode A-1.5/1.5/1.5	Mode B-1.1/1.5/1.2
High-medium -low 1–2–3 High-medium 1–2 High-low1–3 Medium- low 2–3				
switching time	$t_1 = t_0 + D_{12}T_h$ $t_2 = t_0 + D_{13}T_h$ $t_3 = t_0 + D_{y1}T_h$ $t_4 = t_0 + (D_{13} + D_{y3})T_h$ $t_5 = t_0 + (D_{12} + D_{y2})T_h$ $t_6 = t_0 + T_h$	$t_1 = t_0 + D_{13}T_h$ $t_2 = t_0 + D_{12}T_h$ $t_3 = t_0 + D_{y1}T_h$ $t_4 = t_0 + (D_{12} + D_{y2})T_h$ $t_5 = t_0 + (D_{13} + D_{y3})T_h$ $t_6 = t_0 + T_h$	$t_1 = t_0 + D_{y1}T_h$ $t_2 = t_0 + D_{12}T_h$ $t_3 = t_0 + (D_{12} + D_{y2})T_h$ $t_4 = t_0 + D_{13}T_h$ $t_5 = t_0 + (D_{13} + D_{y3})T_h$ $t_6 = t_0 + T_h$	$t_1 = t_0 + D_{12}T_h$ $t_2 = t_0 + D_{y1}T_h$ $t_3 = t_0 + D_{13}T_h$ $t_4 = t_0 + (D_{13} + D_{y3})T_h$ $t_5 = t_0 + (D_{12} + D_{y2})T_h$ $t_6 = t_0 + T_h$
Working mode range	$0 \leq D_{12} \leq D_{13}$ $D_{13} \leq D_{y1} \leq D_{13} + D_{y3}$ $D_{13} + D_{y3} \leq D_{12} + D_{y2} \leq 1$	$0 \leq D_{13} \leq D_{12}$ $D_{12} \leq D_{y1} \leq D_{12} + D_{y2}$ $D_{12} + D_{y2} \leq D_{13} + D_{y3} \leq 1$	$0 \leq D_{y1} \leq D_{12}$ $D_{12} \leq D_{12} + D_{y2} \leq D_{13}$ $D_{13} \leq D_{13} + D_{y3} \leq 1$	$0 \leq D_{12} \leq D_{y1}$ $D_{y1} \leq D_{13} \leq D_{13} + D_{y3}$ $D_{13} + D_{y3} \leq D_{12} + D_{y2} \leq 1$
transmission power	$-\frac{P_{12}}{k_{12}} = D_{12}^2 - 2D_{12}D_{y1} + D_{y1}^2 - D_{y1}D_{y2}$ $-\frac{P_{13}}{k_{13}} = D_{13}^2 - 2D_{13}D_{y1} + D_{y1}^2 - D_{y1}D_{y3}$ $\frac{P_{23}}{k_{23}} = k_{12}^2 D_{y3}\left[2(D_{13} - D_{12}) - D_{y2} + D_{y3}\right]$	$-\frac{P_{12}}{k_{12}} = D_{12}^2 - 2D_{12}D_{y1} + D_{y1}^2 - D_{y1}D_{y2}$ $-\frac{P_{13}}{k_{13}} = D_{13}^2 - 2D_{13}D_{y1} + D_{y1}^2 - D_{y1}D_{y3}$ $-\frac{P_{23}}{k_{23}} = k_{12}^2 D_{y2}\left[2(D_{12} - D_{13}) - D_{y3} + D_{y2}\right]$	$\frac{P_{12}}{k_{12}} = D_{y1}D_{y2}$ $\frac{P_{13}}{k_{13}} = D_{y1}D_{y3}$ $\frac{P_{23}}{k_{23}} = k_{12}^2 D_{y2}D_{y3}$	$-\frac{P_{12}}{k_{12}} = D_{12}^2 - 2D_{12}D_{y1} + D_{y1}^2 - D_{y1}D_{y2}$ $\frac{P_{13}}{k_{13}} = D_{y1}D_{y3}$ $\frac{P_{23}}{k_{23}} = k_{12}^2 D_{y3}\left[2(D_{13} - D_{12}) - D_{y2} + D_{y3}\right]$
Equivalent DAB mode	1→ 2: Mode 1.1 1→ 3: Mode 1.1 2→ 3: Mode 1.2	1→ 2: Mode 1.1 1→ 3: Mode 1.1 2→ 3: Mode 2.4	1→ 2: Mode 1.5 1→ 3: Mode 1.5 2→ 3: Mode 1.5	1→ 2: Mode 1.1 1→ 3: Mode 1.5 2→ 3: Mode 1.2

Table A3. DAB Equivalence and waveform diagram of TAB working mode (2).

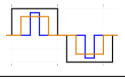
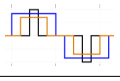
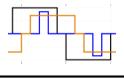
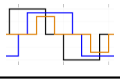
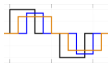
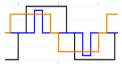
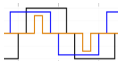
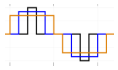
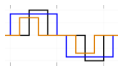
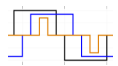
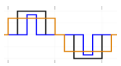
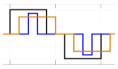
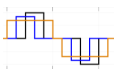
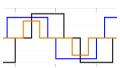
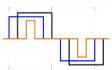
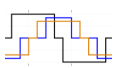
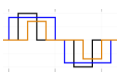
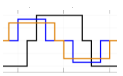
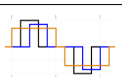
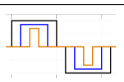
Mode Number	1→2 Equivalent DAB Mode	1→3 Equivalent DAB Mode	2→3 Equivalent DAB Mode	Waveform Port 1: Black/High Port 2: Blue/Mid Port 3: Yellow/Low	Mode Number	1→2 Equivalent DAB Mode	1→3 Equivalent DAB Mode	2→3 Equivalent DAB Mode	Waveform Port 1: Black/High Port 2: Blue/Mid Port 3: Yellow/Low
6	1.2	1.2	2.4		21	2.4	2.4	1.2	
7	1.2	1.4	2.4		22	1.4	1.1	1.2	

Table A3. *Cont.*

Mode Number	1→2 Equivalent DAB Mode	1→3 Equivalent DAB Mode	2→3 Equivalent DAB Mode	Waveform Port 1: Black/High Port 2: Blue/Mid Port 3: Yellow/Low	Mode Number	1→2 Equivalent DAB Mode	1→3 Equivalent DAB Mode	2→3 Equivalent DAB Mode	Waveform Port 1: Black/High Port 2: Blue/Mid Port 3: Yellow/Low
8	1.1	1.1	2.4		23	1.2	2.3	2.4	
9	2.3	1.2	1.2		24	2.4	2.4	2.4	
10	2.4	2.1	1.2		25	1.4	1.2	1.2	
11	1.2	2.4	2.4		26	1.2	1.1	2.4	
12	2.1	2.4	2.4		27	2.3	2.1	1.2	
13	2.1	1.2	1.2		28	1.4	1.4	2.4	
14	2.4	1.2	1.2		29	2.3	2.3	2.4	
15	1.1	2.4	2.4		30	1.2	1.2	1.2	

References

1. Zeng, R.; Zhao, Y.; Zhao, B. A prospective look on research and application of DC power distribution technology. *Proc. CSEE* **2018**, *38*, 6791–6801+7114. (In Chinese)
2. Song, Q.; Zhao, B.; Liu, W. An overview of research on smart DC distribution power network. *Proc. CSEE* **2013**, *33*, 9–19. (In Chinese)
3. Li, Z.; Gao, F.; Zhao, C. Research review of power electronic transformer technologies. *Proc. CSEE* **2018**, *38*, 1274–1289. (In Chinese)
4. Li, J.; Luo, Q.; Luo, T. Efficiency optimization scheme for isolated triple active bridge DC–DC converter with full soft-switching and minimized RMS current. *IEEE Trans. Power Electron.* **2022**, *37*, 9114–9128. [CrossRef]
5. Zhao, C.; Round, S.D.; Kolar, J.W. An isolated three-port bidirectional DC-DC converter with decoupled Power Flow Management. *IEEE Trans. Power Electron.* **2008**, *23*, 2443–2453. [CrossRef]
6. Liu, B.; Shuai, Z.; Xiao, F. Simplified analysis model and optimal control strategy of tripe active bridge converter. *Trans. China Electrotech. Soc.* **2021**, *36*, 2394–2407.
7. Tu, C.; Yu, X.; Xiao, F. A Novel Solution for High-frequency-link AC Current of TAB Converter. *Proc. CSEE* **2021**, *41*, 7740–7750.
8. Huang, J.; Fu, Y.; Lü, X. Control strategy of three-port bidirectional DC-DC converter based on reactive power optimization. *Trans. China Electrotech. Soc.* **2022**, *37*, 2086–2096.
9. Zeng, Y.; Xiao, Z.; Liu, Q. Physics-Informed Deep Transfer Reinforcement Learning Method for the Input-Series Output-Parallel Dual Active Bridge-Based Auxiliary Power Modules in Electrical Aircraft. *IEEE Trans. Transp. Electrif.* **2024**. [CrossRef]
10. Xiao, Z.; Zeng, Y.; Tang, Y. Swift and Seamless Start-Up of DAB Converters in Constant and Variable Frequency Modes. *IEEE Trans. Ind. Electron.* **2024**. [CrossRef]
11. Mou, D.; Luo, Q.; Li, J. Five-Degree-of-Freedom Modulation Scheme for Dual Active Bridge DC–DC Converter. *IEEE Trans. Power Electron.* **2021**, *36*, 10584–10601. [CrossRef]
12. Shao, S.; Jiang, M.; Ye, W.; Li, Y. Optimal Phase-Shift Control to Minimize Reactive Power for a Dual Active Bridge DC–DC Converter. *IEEE Trans. Power Electron.* **2019**, *34*, 10193–10205. [CrossRef]
13. Gu, Q.; Yuan, L.; Nie, J. Current stress minimization of dual-active-bridge DC–DC converter within the whole operating range. *IEEE Emerg. Sel. Top. Power Electron.* **2019**, *7*, 129–142. [CrossRef]
14. Zhao, B.; Song, Q.; Liu, W. Current stress-optimized switching strategy of isolated bidirectional DC-DC converter with dual-phase-shift control. *IEEE Trans. Ind. Electron.* **2013**, *60*, 4458–4467. [CrossRef]
15. Guo, H.; Zhang, X.; Zhao, W. Optimal control strategy of dual active bridge DC-DC converters with extended-phase-shift control. *Proc. CSEE* **2019**, *39*, 3889–3898. (In Chinese)

16. Zhang, L.; Tu, C.; Xiao, F. Intrinsic Law Analysis and Optimization Control of Current Stress in Dual Active Bridge Converter. *Trans. China Electrotech. Soc.* **2024**. [CrossRef]
17. Tong, A.; Hang, L.; Li, G.; Jiang, X. Modeling and analysis of a dual-active-bridge-isolated bidirectional DC/DC converter to minimize rms current with whole operating range. *IEEE Trans. Power Electron.* **2018**, *33*, 5302–5316. [CrossRef]
18. Zhang, X.; Pei, W.; Kong, L. Loss model and analysis of high-frequency-link DC solid state converter for medium voltage AC/DC distribution grid. *Adv. Technol. Electr. Eng. Energy* **2019**, *38*, 43–52.
19. Li, J.; Yuan, L.; Gu, Q. An Efficiency Optimization method in dual active bridge DC-DC converter based on loss model. *Trans. China Electrotech. Soc.* **2017**, *32*, 66–76.
20. Hebala, O.M.; Aboushady, A.A.; Ahmed, K.H. Generic Closed-Loop Controller for Power Regulation in Dual Active Bridge DC-DC Converter With Current Stress Minimization. *IEEE Trans. Ind. Electron.* **2019**, *66*, 4468–4478. [CrossRef]

Disclaimer/Publisher's Note: The statements, opinions and data contained in all publications are solely those of the individual author(s) and contributor(s) and not of MDPI and/or the editor(s). MDPI and/or the editor(s) disclaim responsibility for any injury to people or property resulting from any ideas, methods, instructions or products referred to in the content.